Tetra-Plexing Dual-Broadband/Dual-Polarized Antenna for 5G/6G Millimeter-Wave Systems

Jeongwoo Heo, *Student Member, IEEE,* Byeongjin Kim, *Student Member, IEEE,* Maengchang Kang, *Student Member, IEEE,* Heeyoung Kim, Youngju Lee, and Jungsuek Oh, *Senior Member, IEEE*

***Abstract*—This study introduces a tetra-plexing antenna concept supporting dual-broadband and dual-polarization at 28 and 39 GHz, designed to address prevalent challenges in advanced 5G and 6G communications. Employing a novel tapered multi-slot load (TMSL) and shorting vias, this antenna design not only enhances bandwidth and cross-polarization discrimination (XPD) but also supports the entire mmWave frequency range from n257 to n261. Each radiator accesses a single element, enabling four independent channel paths within one antenna structure. The innovative use of the segmented loop isolator significantly reduces mutual coupling, allowing for effective tetra-plexing. Subsequently, a scalable 1×4 array configuration is introduced, which extends beam steering capabilities up to ±55° at 28 GHz and up to ±38° at 39 GHz, facilitating wide application adaptability. Performance evaluations reveal that simulations show bandwidths of 39.42 % and 19.5 % for 28 GHz and 39 GHz, respectively, while measurements indicate 42.2 % and 28.9 %. XPD improvements are noted above 7 dB and 15 dB at peak levels for 28 GHz and 39 GHz, respectively, with maximum XPD values reaching 23 dB in the LB and 18 dB in the HB. Peak gains are measured at 10.9 dBi and 11.52 dBi in simulations, and 11.27 dBi and 11.8 dBi in measurements for 28 GHz and 39 GHz. By implementing passive branching of signals at the antenna level, the design reduces the load on active circuitry, enhancing overall system performance and positioning the technology as a viable solution for diverse wireless communication applications.**

***Index Terms*—Tetra-plexing, dual-broadband, dual-polarized, millimeter-Wave, scalable, Antenna-in-Package (AiP).**

I. INTRODUCTION

THE millimeter-wave (mmWave) band is recognized for its extensive bandwidth and has emerged as a vital frequency spectrum for advanced 5G and 6G wireless communication systems, fostering substantial technological innovations [1], [2], [3], [4], [5], [6]. The increasing requirements from sectors such as IoT, AR, AI, and autonomous driving necessitate the capacity for real-time data processing, which has heightened interest in mmWave technology, especially due to its low latency [7], [8] [9]. However, the growing data traffic escalates hardware requirements and reduces the space available for front-end modules. In mobile communication antenna design, it remains a challenge to maintain a low profile and small form factor while preserving performance within the constraints of the fabrication process [10], [11]. Techniques like antenna-in-package (AiP) and antenna-in-display (AiD) have been explored to address these challenges [12], [13], [14], [15]. AiP is particularly notable for effectively integrating antennas with mmWave modules by compactly packaging them with active circuitry, which enhances connectivity and system performance by minimizing interconnection losses through multi-layer structures and flip-chip bonding [16].

From the perspective of mmWave bands and integrated wireless communication modules, antennas should meet several critical requirements:

The first key aspect is dual-band operation and broadband capability. According to 3GPP standards, the primary mmWave frequency bands include 24.25–29.5 GHz (n257, n258, and n261) and 37–43.5 GHz (n259 and n260) [17]. Supporting dual-band operation is crucial, and achieving broadband performance is necessary to effectively function across various frequency bands using a single hardware setup. Previous studies have explored dual-band and broadband capabilities using various configurations such as stacked patches, extra parasitic strips, grid patches, hybrid dielectric resonator antennas, and paired ring patches [18], [19], [20], [21], [22]. However, [18] does not support dual bands. [20] and [22] encounter challenges in integrated packaging due to their high profile and complex feed structure, while [21] has difficulties in ensuring manufacturability. Additionally, there is a general need for wider bandwidth.

Furthermore, integrating dual-polarization is vital in AiP modules within wireless communication systems to counteract multipath fading and enhance channel capacity [23], [24], [25]. Employing dual slant polarization instead of traditional vertical polarization improves polarization diversity and structural symmetry. This adjustment significantly reduces issues such as coupling between adjacent antenna elements and disparities in radiation patterns [2]. Moreover, each element must achieve sufficient cross-polarization discrimination (XPD) [26], [27], [28], [29], which should be realized through a straightforward design to maintain compatibility with RFICs. However, ensuring stable XPD performance remains fundamentally challenging in wideband and structurally dense AiP configurations, where tight spatial constraints inherently limit polarization purity. This difficulty becomes even more pronounced in dual-broadband millimeter-wave applications, where maintaining sufficient XPD and achieving wideband operation simultaneously presents significant design challenges. Therefore, it is

This work was supported by the Technology Innovation Program(20022446, Development of active antenna module for 5G private network) funded by the Ministry of Trade, Industry Energy (MOTIE, KOREA) (Corresponding author: Jungsuek Oh, jungsuek@snu.ac.kr).

Jeongwoo Heo, Byeongjin Kim, Maengchang Kang and Jungsuek Oh are with the Institute of New Media and Communications (INMC), Department of Electrical and Computer Engineering, Seoul National University, Seoul, South Korea.

Heeyoung Kim and Youngju Lee are with the Advanced Network Development Office, Electro-Materials Business, Doosan Corporation, Yongin, South Korea.

essential to develop a design approach that addresses these limitations while preserving the compactness necessary for package-level integration.

From the perspective of integrated package design with active circuitry, signal multiplexability is a critical consideration. Most current dual-band AiPs route signals from both bands through a single port to the RFIC, inevitably necessitating active elements for signal branching. This configuration leads to signal loss and increases the overall load on the communication module [30], [31], [32]. Therefore, implementing pre-branching of signals at the antenna level, a passive component, can significantly enhance overall system performance. Studies [33], [34], [35], [36] have shown examples of achieving dual-band port separation using shared aperture and self-diplexing schemes. In [34], Ku/Ka band radiators and Ka band radiators, along with ports, are separated by inter-antenna spacing to branching the signals for each band. In [33], [35], [36] a single radiator is equipped with two ports for different bands to separate the signal paths. However, these designs present the following challenges. First, when separate radiators do not share the same aperture, spatial utilization efficiency is low, limiting performance optimization. Second, in designs like self-diplexing, where the same radiator is used with ports separated by frequency band, supporting dual polarization becomes challenging, and the structural characteristics limit both configuration and performance.

Tetra-plexing addresses these challenges by separating the radiators for each frequency band and supporting them with four independent ports. This configuration enables passive pre-branching of signals, which reduces the reliance on active elements and improves overall system performance. In light of these advantages, this study introduces a tetra-plexing antenna concept that supports dual-broadband and dual-polarization at 28 and 39 GHz. By placing the radiators for both the low band (LB) and high band (HB) within the same element, spatial utilization efficiency is significantly improved, while maintaining four independent signal paths for optimized performance. These antenna cells are then arranged into a 1×4 array configuration. This work distinguishes itself from existing research with the following innovative features:

1) Tetra-plexing significantly improves spatial utilization efficiency by enabling more efficient and compact configurations. This approach also facilitates independent design and optimization for each frequency band, ensuring that radiators from different bands do not significantly interfere with each other. By allowing each band to operate independently, the design achieves greater flexibility in configuring the antenna system to meet specific performance requirements. As a result, design flexibility is enhanced, enabling more versatile and adaptable solutions for both LB and HB.
2) The improved spatial utilization and increased design flexibility enable the implementation of advanced components such as the tapered multi-slot load (TMSL) and shorting via. These components provide an electrical reference and generate multiple resonance modes, significantly improving both broadband and XPD performance. The inclusion of a Reactive Impedance Surface (RIS) further ensures effective impedance matching, allowing the antenna to support dual-band operation and cover the full mmWave frequency range from n257 to n261.
3) The segment loop isolator significantly reduces mutual coupling caused by the close proximity of the radiators, ensuring electrical isolation and maintaining performance integrity.
4) The structure also offers symmetry and flexibility in array configuration. It is scalable, allowing for adaptation to various configurations beyond a 1×4 array, thereby extending scanning range and improving overall performance.

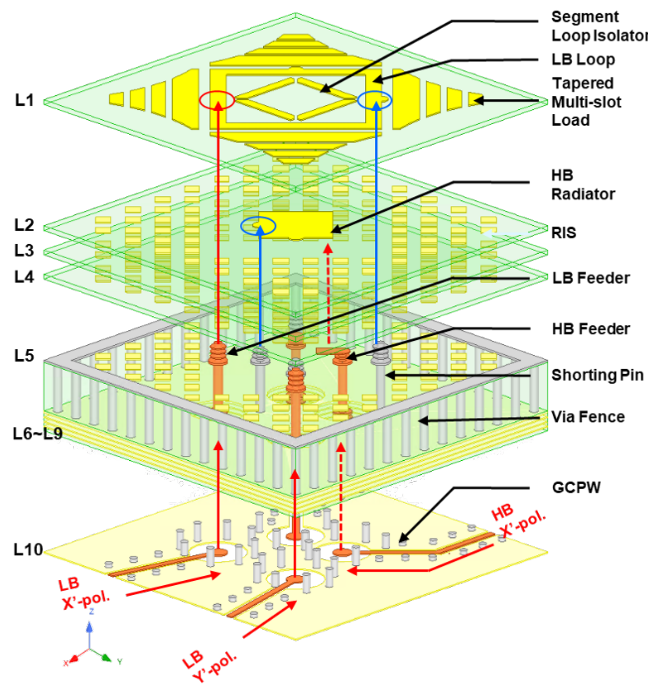

Fig. 1. Geometry of the proposed antenna element. Yellow, orange, and gray indicate conductors, and light green represents dielectric materials.

This work includes the benefits of a simple, compact design with high design flexibility and manufacturability, ensuring high AiP compatibility. Additionally, the wideband response and passive branching through tetra-plexing reduce the load on active circuitry, contributing to overall communication system performance enhancement and promising applications in various fields. This research represents the first attempt to implement such a design in the 28/39 GHz bands, underscoring its innovation and potential impact on future wireless communication systems.

In Section II, the proposed tetra-plexing antenna's PCB configuration and its individual components for each band are introduced. Section III analyzes the operational principles behind the proposed structure's broadband response and XPD performance. In Section IV, the process of minimizing mutual coupling for successful tetra-plexing is analyzed through derivation processes. Section V evaluates the comprehensive performance of the proposed antenna elements, while Section VI provides detailed descriptions of the antenna array

This article has been accepted for publication in IEEE Transactions on Antennas and Propagation. This is the author's version which has not been fully edited and content may change prior to final publication. Citation information: DOI 10.1109/TAP.2025.3570006

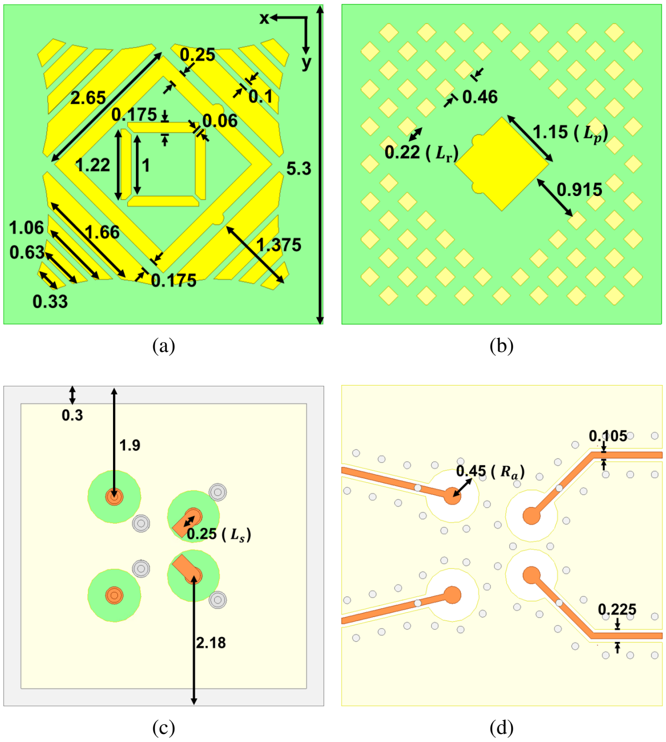

Fig. 2. Top views for each layer with detailed values of structures. (a) Layer 1. (b) Layer 2. (c) Layers 3 to 6 (excluding RIS). (d) Layer 10. (Unit: mm)

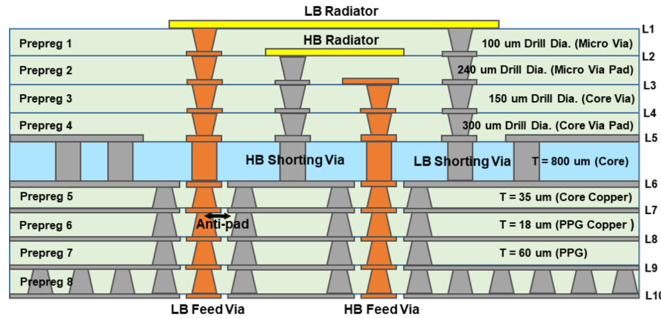

Fig. 3. Antenna stack-up information for a 10-layer PCB process.

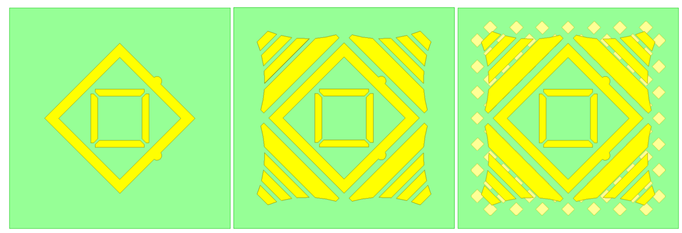

(a) (b) (c)

Fig. 4. Sequential representation of proposed antenna to illustrate each structure's role. (a) Type-A. (b) Type-B with TMSL. (c) Proposed model with both TMSL and RIS.

configuration and measurement results, comparing these with previous research to analyze performance. Finally, Section VII summarizes the paper and consolidates the main findings.

II. Antenna Element Configuration

A. Overall Structure

In this section, the detailed and overall structure of the proposed antenna element will be presented. The configuration of the proposed antenna element is illustrated in Fig. 1. The antenna consists of 10 metal layers (L1-L10). Layers L1-L6 include the radiators and antenna ground, while layers L7-L10 form the feeding network, including vertical transitions. The low-band (LB) antenna is located on L1, featuring a square loop patch and tapered multi-slot load (TMSL). A segment loop isolator separates the LB and high-band (HB) antennas in the center. The HB antenna, with a rectangular patch shape, is located on L2. To perform impedance matching, Reactive Impedance Surface (RIS) is placed parallel to the HB patch, extending to L5. A metallic via fence runs from L5 to L6 to prevent coupling and field leakage between antenna cells in the core layer. A loop on L5 covers and separates each antenna cell. Layers L6-L9 contain a metal plate with an anti-pad for the feeding section, and L10 features a Coplanar Waveguide with Ground (GCPW) connected via feeder for signal transmission, forming a vertical transition. Each radiator is slant polarized at a ±45°, with two ports per band for dual polarization operation. As shown in Fig. 3, vias running from L1 to L10 drive the LB antenna. The HB antenna is fed by vias extending to the layer just below the radiators, with L-shaped probes applied. Additionally, shorting vias are introduced opposite the feeding vias, connecting the radiators to the antenna ground on L6, forming the electrical reference, with further details provided later.

The main parameters of each structure are shown in Fig. 2. The antenna cell has overall dimensions of 5.3 × 5.3 × 1.494 mm^3, including the metal thickness. It is designed and fabricated using PCB manufacturing processes. The core is located at the center, and each copper layer is connected through prepreg (PPG) to form a total of 9 substrate layers. The core and PPG have thicknesses of 800 μm and 60 μm, with core copper and PPG copper having thicknesses of 35 μm and 18 μm, respectively. The antenna was fabricated using the DS7409HG-KN substrate manufactured by DOOSAN. The relative dielectric permittivity (ϵ_r) of the core and PPG is 3.4 and 3.26, with loss tangents of 0.004 and 0.0053. The vertical transition for feeding each antenna consists of a signal via at the center, surrounded by several ground vias. In layers L6 to L10, an anti-pad is applied between the pad barrel and the plate to form a coaxial signal path. For these metallic vias, the core substrate uses through-hole vias with a diameter of 150 μm and capture pads with a diameter of 300 μm on the top and bottom. For the PPG, cone-shaped microvias are used, with a diameter of 100 μm and capture pads with a diameter of 240 μm.

B. Performance Enhancement in Dual-Band Operation

The proposed structure is designed for dual-broadband operation as follows. A square loop patch supports the low band (LB), while a separate square patch antenna supports the high band (HB). However, the single resonance mode in the LB does not provide sufficient bandwidth. To address this, a tapered multi-slot load (TMSL) is newly introduced. This

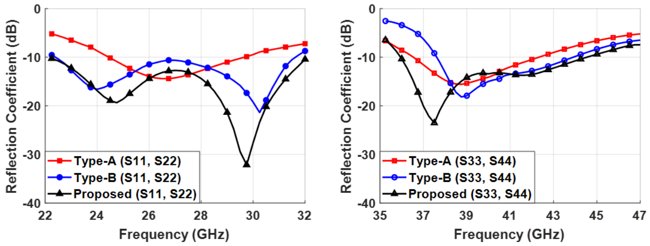

(a) (b)

Fig. 5. Simulated reflection coefficients for Type-A, Type-B, and the proposed structure. The results are identical for each polarization. (a) LB (S11 = X′-pol., S22 = Y′-pol.). (b) HB (S33 = X′-pol., S44 = Y′-pol.).

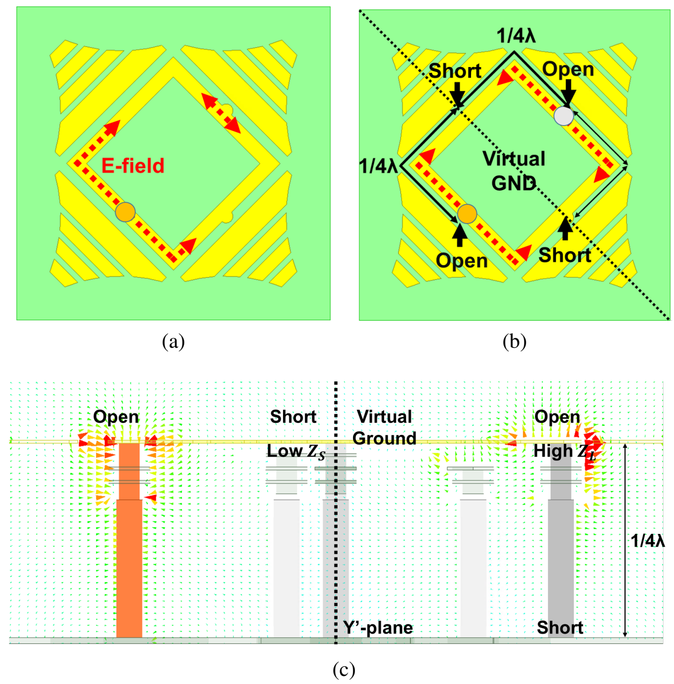

Fig. 6. E-field distribution of (a) a typical loop-shaped antenna and (b) the proposed antenna with the shorting via, including the electrical state. (c) Cross-sectional view showing the electrical state and impedance.

structure induces a new resonance and has a tapered shape on both sides exponentially, with a constant gap, as depicted in Fig. 1, symmetrically placed near the LB loop patch. For comparison, Fig. 4(a) shows the top view of the initial model without the TMSL, and Fig. 4(b) shows the top view of the model with the TMSL. Finally, to achieve additional bandwidth and impedance matching, the proposed structure with a reactive impedance surface (RIS) is depicted in Fig. 4(c). Fig. 5 shows the simulated reflection coefficient results for the three cases mentioned above. Fig. 5(a) and Fig. 5(b) depict the reflection coefficients S11 and S33 for the LB and HB, respectively, with each S11 and S33 related to the X′-polarization (ϕ = -45°). Since the antenna is symmetrically structured, the Y′-polarization ($\phi = 45°$) components, S22 and S44, exhibit identical responses at each frequency. For the LB, the initial model shows a single resonance at the center due to the loop patch antenna, with a reflection coefficient below -10 dB (S11 < -10 dB). When the TMSL is introduced, as shown in Fig. 4(b), two resonances occur in the LB, and the blue solid line shows a bandwidth response that is twice as wide as the red solid line. Additionally, the black solid line clearly demonstrates the effectiveness of the proposed structure. Due to the RIS located on each metal layer of the antenna section, the resonance centers near 25 GHz and 29 GHz are more pronounced, resulting in significantly improved reflection coefficient responses across the entire band. In the case of the HB reflection coefficient S33 depicted in Fig. 5(b), the initial model shows resonance due to the square patch located at L2, represented by the red dashed line. The addition of the TMSL has a minimal effect, as shown by the blue dashed line. Similarly, for the HB, the RIS performs effective impedance matching, resulting in improved bandwidth performance, as shown by the black dashed line. These results demonstrate that the newly introduced TMSL effectively achieves a wideband response. Additionally, the minimal impact on the separate bands proves the improved design flexibility. The RIS provides additional matching parameters for both bands, facilitating optimal bandwidth performance.

III. The Principle of Multi-Mode Response

A. Electrical Reference due to Shorting Via

In the proposed structure, the resonance modes of each band are independent yet designed to exhibit identical radiation patterns. This section analyzes how the structure achieves successful dual-broadband operation and enhanced cross-polarization discrimination (XPD), leading to high antenna performance.

First and foremost, to ensure efficient coverage, optimal gain, and enhanced antenna capability, the proposed design is made equivalent to a cavity model with open-short-open electrical states and excites the TM_{10} mode and quasi-TM_{30} mode. Consequently, this ensures a broadside radiation pattern across the entire operating band. Furthermore, by positioning each mode in adjacent frequency bands and eliminating unnecessary modes, the design achieves not only broadband operation but also maintains the gain bandwidth to meet performance requirements. These aspects are detailed in the subsequent section.

The proposed structure uses a loop-shaped LB antenna to prevent interference with the radiation pattern in other frequency bands. However, this design requires certain improvements. Fig. 6(a) illustrates a typical loop-shaped antenna and its E-field distribution. The antenna is partially asymmetrical, with the field path formed along the loop due to its open-center structure, making it sensitive to asymmetry. This makes it difficult to establish an electrical reference at the center, resulting in an unbalanced and asymmetrical field distribution. These factors lead to distorted radiation patterns, shifted resonant frequencies, and significant negative impacts on XPD.

To address these issues, shorting vias are introduced to establish a clear electrical reference. Fig. 6(b) depicts the setup, with the feed via (X′-pol) highlighted in orange and the shorting via in gray. The reference begins from the antenna ground on the sixth layer. The gray point is separated from

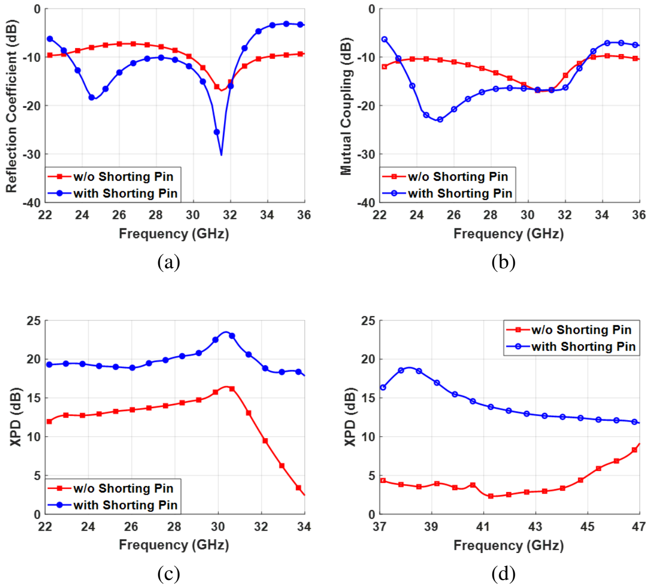

Fig. 7. Simulation comparison of S-parameters for the proposed structure with and without shorting vias. (a) Reflection coefficient (S11). (b) Polarization isolation (S21). (c) XPD for the LB. (d) XPD for the HB with and without HB shorting vias.

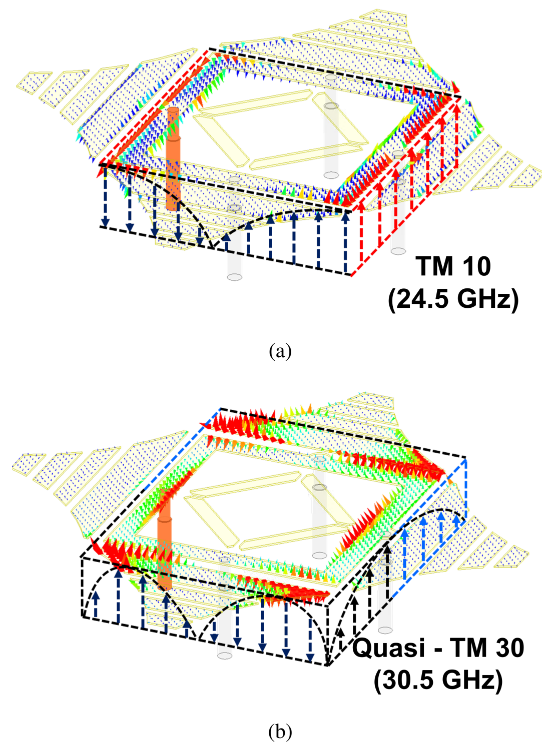

Fig. 8. E-field distribution for LB resonances. (a) 24.5 GHz (TM_{10}) and (b) 30.5 GHz (quasi-TM_{30}).

this ground by a quarter-wavelength, resulting in an open state. Similarly, the center points of the loop's sides that are a quarter-wavelength away from the gray point are in a short state, and the feed point, being a quarter-wavelength away from the short point, is in an open state. This arrangement creates a clear reference and an electrically symmetrical structure, with virtual grounds forming at the centers of the shorted sides, as indicated by the electrical state and E-field distribution in Fig. 6(b). Consequently, the E-field distribution is also symmetrical.

Fig. 6(c) provides a cross-sectional view showing the virtual ground, electrical state, and impedance. It is here that the shorting vias are described as approximately a quarter-wavelength long. The center of the side with the shorting via is electrically connected to the shorted ground and, being separated by the height of the shorting via, has a very high impedance Z_L, resembling an open state. Consequently, the centers of the sides parallel to the polarization direction are electrically separated by a quarter-wavelength from this high Z_L and are in a short state Z_S. The side opposite the shorting via is also in an open state. The cross-section reveals the E-field distribution within the structure. Starting from the shorting via, the grounded side consistently shows field zero, while the upper part displays field maxima, indicating it is in an open state. The center of the cross-section forms a clear virtual ground with field zero centered on the Y′-plane. The feed via side shows field maxima, indicating an open state with a phase opposite to the other side.

Fig. 8 further corroborates these findings. Starting from the field maxima, a perfectly symmetrical half-wavelength mode resonance with a uniform field distribution and field zero at the center is observed.

The virtual ground formed by the shorting via provides high isolation between polarizations and significantly improves XPD. This is because the other feed via for dual-polarization operation is positioned at the field zero point for orthogonal polarization components [37], [38], [39]. Additionally, unintended resonances can be eliminated through the virtual ground [40]. Moreover, this scheme allows for dual-polarization by applying the identical scheme to the orthogonal polarization without interference. The shorting vias are also applied to the HB port.

Fig. 7 illustrates the improved reflection coefficients, X′-Y′ port isolation, and XPD performance. In Fig. 7(a), the reflection coefficient performance is shown with two dominant mode resonances below -10 dB. An unstable mode around 22 GHz, initially out-of-band, has been brought into the in-band range, and an unintended mode at higher frequencies is successfully eliminated. Fig. 7(b) indicates that the isolation has improved from 10.3 dB to over 23 dB in the maximum improvement region. The XPD has also significantly improved, with a minimum enhancement of 7 dB for LB and an improvement ranging from 7 dB to over 16 dB for HB. These results validate the performance of the proposed structure.

The impedance matching of the feed via is performed as follows: the feed via is connected to the bottom layer, providing inductance, while the anti-pad between the via pad and the metal plate has its own capacitance. Impedance matching is achieved by adjusting the diameter R_a of the anti-pad [16].

B. TM_{10} Mode and Quasi-TM_{30} Mode

Fig. 8 shows the E-field distribution of the main resonance modes of the LB. At 24.5 GHz, Fig. 8(a) displays a symmetric

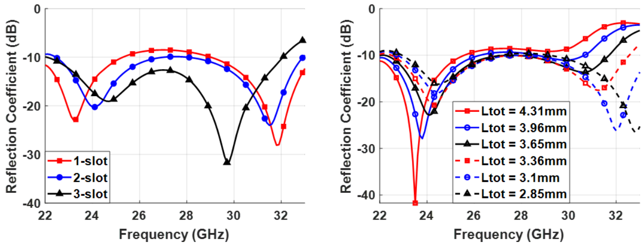

(a) (b)

Fig. 9. Reflection coefficient results (S11) with varying parameters. (a) Number of slots per TMSL. (b) Total physical length of slots in each TMSL (L_{tot}).

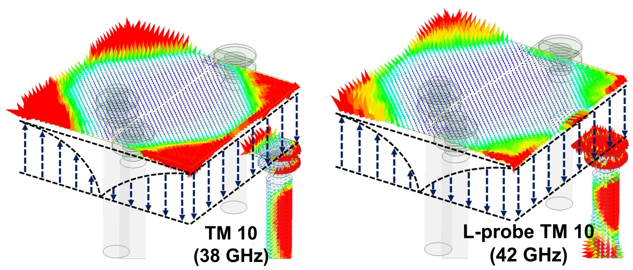

(a) (b)

Fig. 10. E-field distribution of HB rectangular patch with L-shaped probe at (a) 38 GHz and (b) 42 GHz.

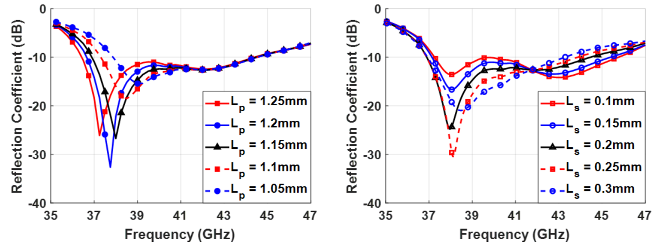

(a) (b)

Fig. 11. Simulation results of HB reflection coefficients (S33) with variations in each parameter: (a) HB square patch size (L_p) and (b) L-probe stub length (L_s).

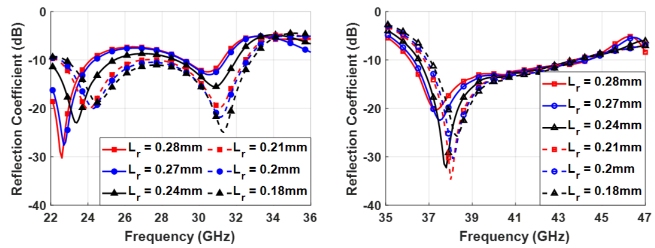

(a) (b)

Fig. 12. Reflection coefficient results with changes in RIS cell size L_r, with cell spacing fixed at 0.46 mm. (a) S11 (LB). (b) S33 (HB).

field distributed along the loop boundary, exciting the TM_{10} mode with two maximum fields along the cavity. This field path forms a half-wavelength resonance around the loop.

Typically, placing higher-order modes in adjacent bands requires much longer electrical lengths compared to fundamental modes. Achieving this with a single resonator configuration is difficult, and combining two modes presents additional challenges. The TMSL provides additional effective electrical paths and greater design flexibility, making it an optimal solution.

Fig. 8(b) shows the quasi-TM_{30} mode excited using the TMSL. This mode also has a field zero at the center due to the virtual ground, with six symmetrical E-field maxima. The field maxima in the TMSL are coupled out-of-phase from the adjacent loop edges and form field paths along the TMSL's edges and slots, resulting in the excitation of the quasi-TM_{30} mode.

Fig. 9(a) shows the reflection coefficients based on the number of slots in the TMSL. As the number of slots increases, the resonance frequency of the quasi-TM_{30} mode shifts to a lower frequency. This indicates that the slots create an effective electrical path and contribute to the mode operation. Additionally, it suggests that adjusting the number of slots allows for the synthesis of different modes.

To achieve the optimal effective electrical length, an exponential tapered shape was chosen. This shape allows for the adjustment of the slopes on both sides, which can be viewed as the order of the exponential function, to set the optimal weight for each slot and achieve the desired characteristics. This design is based on the field property that slots closer to the center contribute more to the mode, while outer slots have less influence. The exponential function has a steeper gradient near the reference axis and a decreasing gradient as it moves away, allowing the structure to provide optimal conditions through these gradient changes. Additionally, based on the derived weights, the depth of both sides can be adjusted to ensure parameter changes occur with appropriate resolution. This depth can be viewed as the coefficient of the exponential function, making optimization easier.

The structure was designed to follow the exponential function curve, and Fig. 9(b) shows the reflection coefficient plotted against the total slot length, L_{tot}, for each TMSL. As the gradient becomes steeper, L_{tot} decreases, and as the gradient becomes shallower, L_{tot} increases. This change in effective electrical length results in a shift in the quasi-TM_{30} mode's resonance frequency. Laborious and extensive parameter studies were conducted to achieve optimal weight distribution. Simulation results confirmed that as L_{tot} decreases, the mode shifts to higher frequencies.

C. High Band Response

An indirect feeding method using an L-shaped probe is adopted for the HB antenna feed. Coupling to the square patch occurs through a stub located at the top of the via, and the coupling coefficient can be adjusted by modifying the stub length. Additionally, a shorting via is placed opposite each L-shaped probe. Fig. 10 shows the E-field distribution of the HB antenna. These modes appear to result from the interactions between the patch and monopole [16]. Fig. 11 illustrates the reflection coefficients for different square patch sizes and stub lengths.

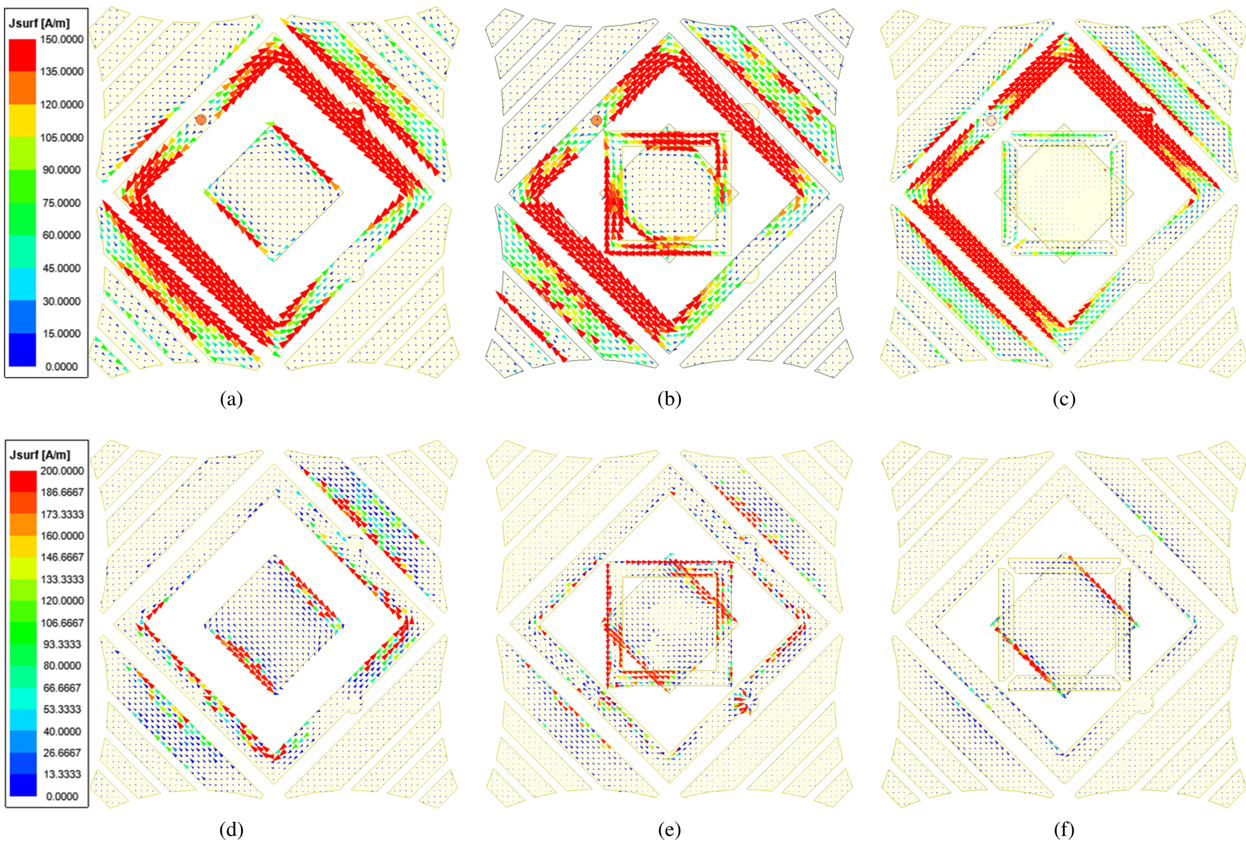

Fig. 13. Surface current distribution at 28 GHz for (a) without segment loop isolator, (b) unsegmented loop and (c) proposed structure; and at 39 GHz for (d) without isolator, (e) unsegmented loop, and (f) proposed structure.

D. Reactive Impedance Surface (RIS)

To achieve additional design flexibility and impedance matching, a Reactive Impedance Surface (RIS) was introduced. Identical structures were installed from layers 2 to 5, enhancing performance and ensuring high manufacturability by maintaining the required copper ratio for the PCB manufacturing process [2]. The RIS consists of square periodic structures of the same size, arranged parallel to the radiating element. These structures have inter-period and inter-layer capacitances, represented as effective capacitance C_r. Additionally, the capacitance between the radiating element and RIS (C_p) and between RIS and the ground (C_g) are considered. Since these capacitances are dominant, other smaller values can be ignored. As the field propagates along the z-axis, it can be modeled using a transmission line model. Matching can be achieved by adjusting the size and spacing of the periodic structure cells. Fig. 12 shows the reflection coefficient variations with changes in cell size, while the spacing between each RIS cell remains constant.

IV. Mutual Coupling Reduction for Tetra-Plexing

In structurally dense antenna systems, such as millimeter-wave AiP implementations, radiating elements are closely packed within a compact aperture, making mutual coupling a significant concern. This issue is further amplified in dual-band configurations, where radiators for different frequencies coexist. In such cases, inter-band coupling can lead to signal leakage between ports, degrading antenna efficiency and overall system performance—especially in millimeter-wave applications where high efficiency is essential.

To address this issue, the proposed design incorporates a segment loop isolator that mitigates inter-band coupling through a balancing effect. This section verifies its effectiveness by comparing three design configurations for the LB and HB cases, respectively, and presenting field analysis to clarify the underlying suppression mechanism. The observed improvements in isolation between the LB and HB ports are then evaluated in relation to antenna efficiency, providing further insight into the practical implications of enhanced inter-band isolation.

First, Fig. 13(a) presents the case without a segment loop isolator and the associated surface current distribution for the LB configuration. In this case, the close physical proximity of the radiators leads to direct mutual coupling. As a result, the surface current flowing along the LB loop induces a strong inverted-phase surface current in the central rectangular patch, significantly degrading inter-band isolation.

Next, Fig. 13(b) introduces an unsegmented loop on layer 1 as an intermediate model for mechanism analysis. This loop is tilted 45° relative to the other radiator. Mutual coupling induces a current in the central loop with an opposite phase to that of the LB radiator. However, a strong surface current is still observed in the HB patch, indicating that the inter-band coupling problem remains unresolved in this configuration.

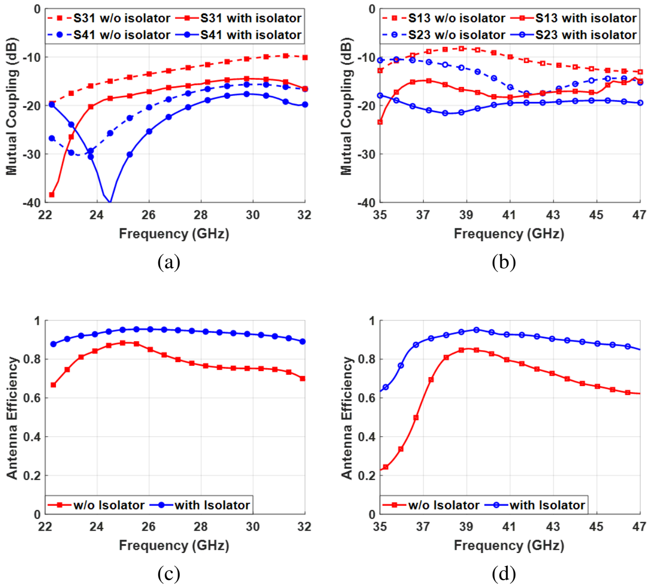

Fig. 14. (a), (b) Simulated port isolation between LB and HB for the configurations shown in Fig. 13(a), (c) and Fig. 13(d), (f), respectively. (c), (d) Corresponding antenna efficiencies with and without the segment loop isolator for LB and HB.

To resolve this issue, the segment loop isolator is introduced, as shown in Fig. 13(c). The continuous loop is divided into four segments with open edges. In this configuration, the in-phase current from the LB radiator enters the segment loop through the slot, while the loop current remains out of phase with the LB resonance. These two currents interact and cancel each other due to their phase opposition, effectively suppressing the current coupled into the HB patch. This balancing effect enables significant improvement in inter-band isolation.

To evaluate whether the same mechanism is observed in the HB case, Fig. 13(d)–(f) present the corresponding surface current distributions. Fig. 13(d) shows the baseline configuration without a loop structure when the HB radiator is active. As observed, strong mutual coupling occurs due to the close proximity between radiators, inducing a surface current in the LB radiator and degrading inter-band isolation.

In Fig. 13(e), which shows the unsegmented loop configuration, mutual coupling induces a current in the central loop with an opposite phase to that of the HB resonance. However, surface current still remains in the LB radiator.

In Fig. 13(f), the segmented loop isolator is applied in the HB case. The in-phase current from the HB radiator enters the segment loop, while the loop current remains out of phase with the HB resonance. Due to this phase opposition, the two currents cancel each other out, and surface current is effectively suppressed in the LB radiator. This confirms that the same balancing effect observed in the LB case also applies in the HB case, enabling effective bidirectional isolation.

Fig. 14(a) and Fig. 14(b) compare the isolation between the LB and HB ports for the cases analyzed in Fig. 13(a), (c) and Fig. 13(d), (f), respectively. These results demonstrate that the introduction of the segment loop isolator effectively suppresses mutual coupling. Notably, the isolation level remains above 15 dB across the entire operating bandwidth, confirming the effectiveness of the proposed structure in maintaining clear separation between frequency bands.

Fig. 14(c) and Fig. 14(d) further present the corresponding antenna efficiencies for the LB and HB cases, with and without the segment loop isolator. The results indicate that mitigating inter-band coupling leads to a measurable improvement in radiation efficiency, with in-band values increasing by 0.1 to over 0.2. When the isolator is applied, the antenna achieves consistently high efficiency in the range of 0.9 to 0.95 across both bands.

These improvements confirm the practical advantages of the proposed approach, enabling four fully independent signal paths through enhanced isolation and efficient dual-band, dual-polarized operation—thereby validating the feasibility of stable tetra-plexing functionality in compact millimeter-wave AiP environments.

V. Antenna Cell Performances

The final S-parameter characteristics of the proposed antenna cell are shown in Fig. 15(a) and (b). For the LB band, the reflection coefficient is below -10 dB from 22 GHz to 32 GHz, and for the HB band, it is from 36 GHz to 44.8 GHz. The isolation between X′-Y′ pol. and between the bands is also presented, with inter-band port isolation exceeding 15 dB across the entire operational bandwidth. Fig. 15(c) to (f) display the radiation patterns for each band, including the Co-pol. and X-pol. at 25 GHz, 30 GHz, 39 GHz, and 43 GHz. The peak gains for each frequency band are 5.89 dBi, 5.34 dBi, 5.21 dBi, and 4.9 dBi, respectively. As explained in the previous section, a broadside pattern is observed across the entire frequency range. The cross-polarization performance, as summarized in Fig. 7, is significantly improved and noteworthy. Furthermore, antenna efficiency has been evaluated to provide a more comprehensive assessment of the proposed design. The results in Fig. 15(g) and (h) show consistently high efficiency levels of approximately 0.9–0.95 across the operational bandwidths for both the LB and HB bands.

VI. Antenna Array and Measurement Results

A. Fabrication and Measurement

The proposed antenna is configured in a 1×4 linear array for coverage through beam steering, aligned along the y-axis. The spacing between each cell is 0.44 λ_0 at the center frequency of the LB, with a total length of 21.1 mm. Additionally, connectors are attached to the GCPW of the bottom layer for antenna feeding. While additional substrate area is needed for the connectors, this has minimal impact on antenna performance. Fig. 16(a) and (b) show the array antenna constructed to evaluate the proposed structure's performance. The S-parameters and radiation patterns are measured inside an anechoic chamber, as shown in Fig. 16(c).

Fig. 17 presents the simulated and measured S-parameter results of the array antenna. Due to the antenna's symmetrical structure, both polarizations exhibit the same characteristics, so the results are shown based on X′-pol. For reflection

This article has been accepted for publication in IEEE Transactions on Antennas and Propagation. This is the author's version which has not been fully edited and content may change prior to final publication. Citation information: DOI 10.1109/TAP.2025.3570006

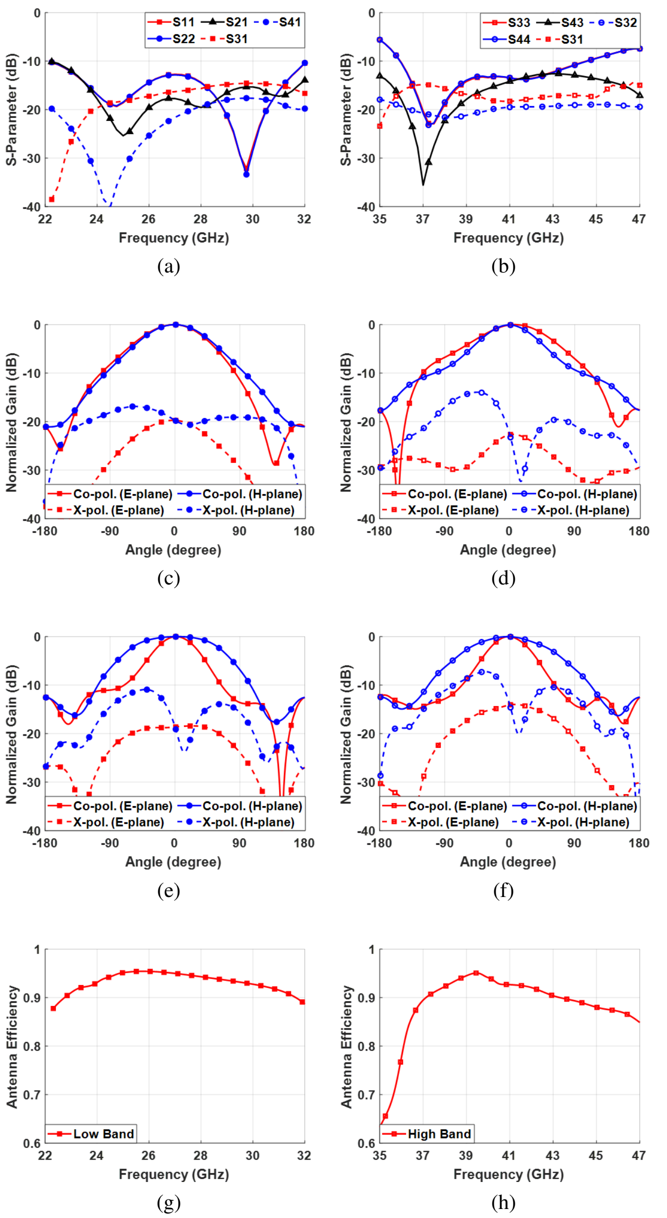

Fig. 15. Simulated comprehensive S-parameter results for the proposed antenna element: (a) S-parameters at LB, (b) S-parameters at HB and total normalized radiation patterns at (c) 25 GHz, (d) 30 GHz, (e) 39 GHz and (f) 43 GHz; and corresponding radiation efficiencies for (g) LB and (h) HB.

coefficients below -10 dB, the simulation results show a bandwidth of 22 GHz – 32.8 GHz for the LB and 37 GHz – 45 GHz for the HB. The measured results show 21.5 GHz – 33 GHz for the LB and 35 GHz – 46.8 GHz for the HB. Fig. 17(c) and (d) display the isolation results between ports, specifically between the first cell and its adjacent cell. The port numbers follow the previously indicated order. The achieved isolation demonstrates sufficient performance within the bandwidth, with inter-band isolation within each antenna cell showing at least 15 dB. These results indicate that the proposed structure successfully achieves inter-band port isolation and wideband performance.

The radiation patterns for each frequency band are shown

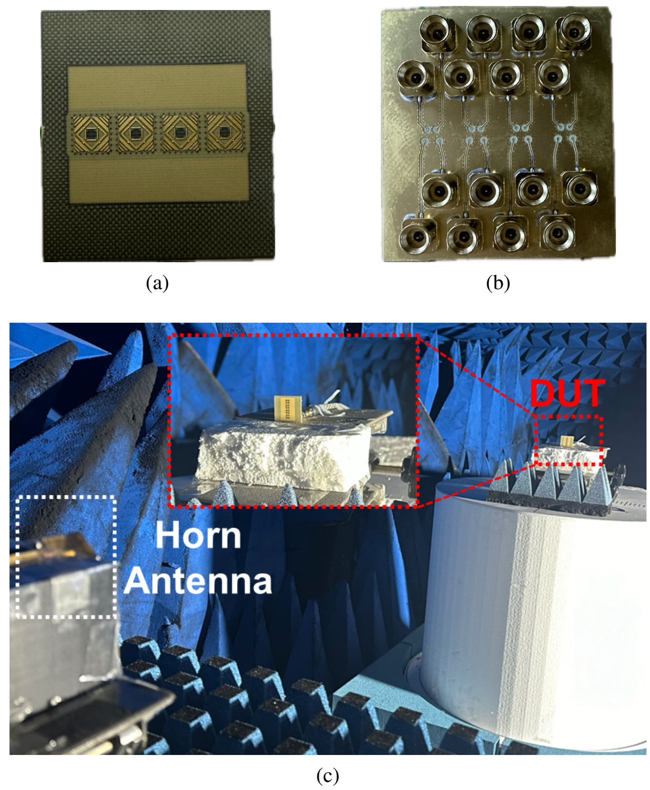

Fig. 16. Fabricated 1×4 array antenna. (a) Top view. (b) Bottom view and (c) measurement setup in anechoic chamber.

in Fig. 18. Each band consists of two main resonances, and the patterns are plotted accordingly. Fig. 18(a) and (b) show the normalized radiation patterns for 25 GHz and 30 GHz, while Fig. 18(b) and (d) display the patterns for 39 GHz and 43 GHz. The maximum gain for the LB is 10.7 dBi and 10.8 dBi in the simulations, and 10.74 dBi and 10.79 dBi in the measurements. For the HB, the simulations show maximum gains of 11.46 dBi and 10.62 dBi, while the measurements show gains of 11.45 dBi and 11.3 dBi. The XPD for the LB are 18.65 dB and 23 dB in the simulations, and 20.15 dB and 25 dB in the measurements. For the HB, the XPD values are 18 dB and 13.8 dB in the simulations, and 21 dB and 16.5 dB in the measurements. Fig. 19 summarizes the maximum gain across the entire frequency band, showing that the gain bandwidth is satisfied across all bands except for the lowest part of each band.

The measured bandwidth and gain are slightly higher than the simulated results, which may be attributed to structural differences between the fabricated sample and the simulation model. Specifically, the additional space needed for connector attachment resulted in a larger ground and aperture area, as seen in Fig. 16(a) and (b). In addition, minor fabrication tolerances may have led to slight deviations from the intended geometry, potentially improving the impedance matching.

B. Beam Steering

Fig. 20 shows the beam steering performance of the simulated and measured radiation patterns. The frequencies for each pattern are the same as previously discussed, and the

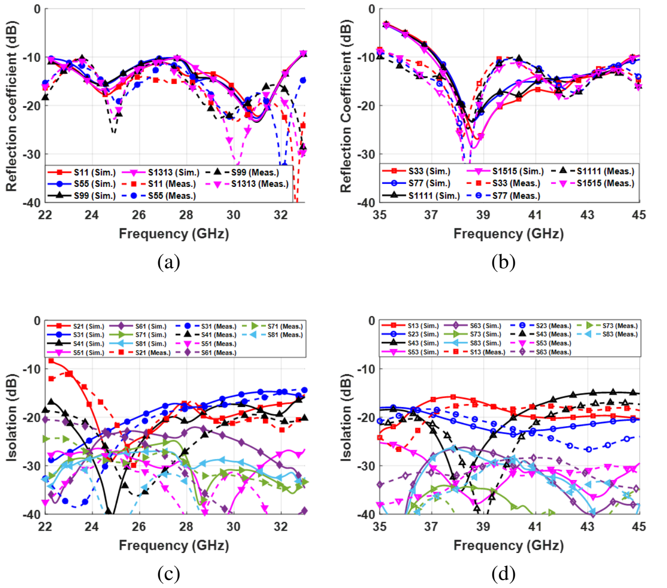

Fig. 17. Simulation and measured results of the proposed 1×4 array antenna. (a) Reflection coefficient in the LB and (b) HB. Port isolation for (c) LB and (d) HB.

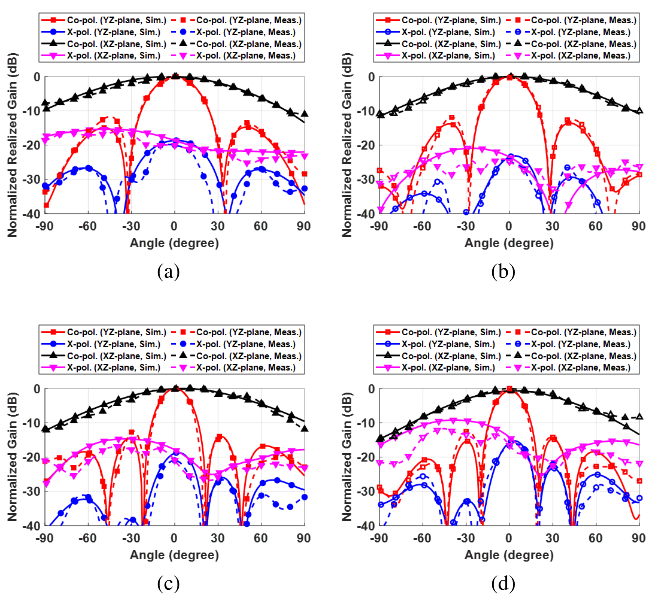

Fig. 18. Normalized radiation patterns for each frequency band, both simulated and measured: (a) 25 GHz. (b) 30 GHz. (c) 39 GHz. (d) 43 GHz.

angles of the peak points are indicated. At 25 GHz, results are shown for 0°, 15°, 30°, and 55°, with a 3 dB scan angle of ±55°. At 30 GHz, results are shown for 0°, 15°, 30°, and 50°, with a maximum beam steering angle of ±50°. For the HB, 39 GHz results are shown for 0°, 15°, 30°, and 38°, with a maximum beam steering angle of ±38°. At 43 GHz, results are shown for 0°, 15°, 25°, and 30°, with a maximum beam steering angle of ±30°. Overall, there are slight discrepancies, such as minor frequency shifts between the simulation and measurement results, but they are generally in good agreement.

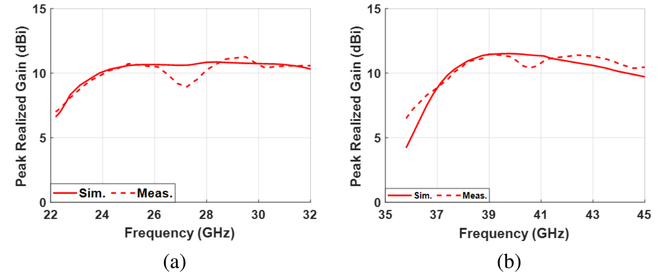

Fig. 19. Measured and simulated peak gain of the proposed antenna. (a) LB. (b) HB.

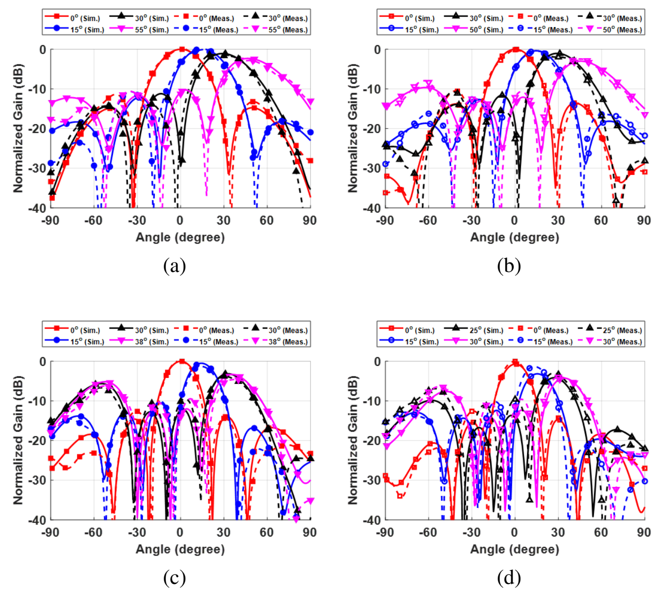

Fig. 20. Measured and simulated beam-steering radiation patterns for each frequency band: (a) 25 GHz, (b) 30 GHz, (c) 39 GHz and (d) 43 GHz.

C. Comparison

Table I lists previously studied 5G/6G mmWave antennas and other array antennas. Study [18] allows for flexible array configuration but only supports a single band and single polarization, providing only one channel. Studies [19], [20], [21], [22] support dual-band and dual-polarization but cannot separate the bands, offering only two channels. Specifically, comparing study [20] with the proposed structure, [20] has limitations in array antenna configuration because it is not scalable.

To achieve wide bandwidth, previous studies combined multiple radiators or used parasitic strips. Compared to these, the proposed antenna is notable for its innovative design that supports the entire allocated mmWave band while delivering outstanding bandwidth performance and achieving significantly higher overall performance. Studies [33], [34], [35] used circulators or shared aperture schemes to secure four channels but faced challenges due to structural constraints. In comparison, the proposed structure achieves tetra-plexability with a more flexible and compact design, is scalable, and achieves wide bandwidth and 3 dB scan angles, among other

TABLE I
COMPARISON

Ref.	Frequency (GHz)	Dimension* ($\lambda_0^L \times \lambda_0^W \times \lambda_0^H$)	Configuration (Scalability)	Polarization	Bandwidth (%)	Peak Gain (dBi)	3 dB Scan Angle (degree)	Number of Channel (Multiplexability)
[18]	26	3.84×3.84×0.22	8×8 (Supported)	Single LP	19.2	16.4	±45°	1 (N.A)
[19]	28/39	1.58×0.36×0.093	1×4 (Supported)	Dual LP	15.38/15.38	11.1/11.25	±60°/±45°	2 (N.A)
[20]	28/44	1.28×1.28×0.16	2×2 (N.A)	Dual LP	30.5/9.0	14.8/14.1	-51°∼43° -28°∼30°	2 (N.A)
[21]	28/39	0.34×0.36×0.10	Single (Supported)	Dual LP	14.11/12.56	6.8/6.4	±50°/±40°	2 (N.A)
[22]	28/39	0.86×0.86×0.16	2×2 (Supported)	Dual LP	19.5/7.8	7.0/10.0	N.A	2 (N.A)
[35]	7.5/8.1	2.5×2.5×0.073	4×4 (N.A)	Dual CP	5/6.2	14.5/15	N.A	2 (Supported)
[33]	3.5/26	3.17×2.75×0.003	2×4 (N.A)	Single LP	11.7/11.9	5/12.9	±25°	2 (Supported)
[34]	14/28	1.47×0.47×0.1	1×3/1×5 (N.A)	Dual LP	7.5/2	10.1/12.1	±43°/±45°	4 (Supported)
This work	**28/39**	**1.76×0.44×0.12**	**1×4 (Supported)**	**Dual LP**	**42.2/28.9 (Meas.)**	**11.27/11.8 (Meas.)**	**±55°/±50° (25/30 GHz) ±38°±30° (39/43 GHz)**	**4 (Supported)**

* Refers to the wavelength of the center frequency in the lower band.

improved radiation performance.

This comparative study demonstrates that the proposed antenna excels in various aspects, particularly in bandwidth, where it outperforms comparable designs. Tetra-plexing ensures superior performance, offering a more flexible and scalable design, which is easy to integrate into devices and highly suitable for 5G/6G AiP applications.

VII. CONCLUSION

In this paper, we propose a tetra-plexing dual-band dual-polarized antenna with four separate channel paths for the mmWave band, along with an array antenna using this design. This innovative approach uses a loop-shaped antenna with a shorting via for LB resonance, providing a clear electrical reference and successfully securing the fundamental TM_{10} mode and high XPD performance. The introduction of a novel TMSL to excite the quasi-TM_{30} mode, combined with a RIS, has enabled us to achieve wideband performance across the full mmWave spectrum. Additionally, the HB patch with an L-shaped probe shares a single element to effectively separate the LB-HB channel paths. A segment loop isolator significantly reduces mutual coupling between the radiating elements, ensuring sufficient isolation. Importantly, each component's presence or absence minimally affects the other bands, allowing for independent design and ensuring design flexibility. This design also achieves passive pre-branching, reducing the reliance on active components and improving the overall performance of the wireless communication module.

Configured as a 1×4 array, the proposed antenna demonstrates high beam steering performance, which has been verified through measurements. Additionally, the design is scalable, allowing for further expansion into larger arrays, making it adaptable for a wider range of applications.

Simulation results indicated bandwidths of 39.42 % and 19.5 % for each band, with measurements showing 42.2 % and 28.9 %. XPD improvements exceeded 7 dB and 15 dB at peak levels. We also achieved isolation above 15 dB and peak gains of 10.9 dBi and 11.52 dBi in simulations, with measured gains of 11.27 dBi and 11.8 dBi. Beam steering performance recorded peak angles of ±55°, ±50°, ±38°, and ±30° for each band.

Beyond these performance metrics, the proposed antenna's scalability and compactness demonstrate high feasibility for antenna-in-package (AiP) applications. This design holds significant potential for expansion into other mmWave wireless communication applications, highlighting its impact on future technologies.

REFERENCES

[1] W. Hong, Z. H. Jiang, C. Yu, D. Hou, H. Wang, C. Guo, Y. Hu, L. Kuai, Y. Yu, Z. Jiang, Z. Chen, J. Chen, Z. Yu, J. Zhai, N. Zhang, L. Tian, F. Wu, G. Yang, Z.-C. Hao, and J. Y. Zhou, "The role of millimeter-wave technologies in 5g/6g wireless communications," *IEEE J. Microwaves*, vol. 1, no. 1, pp. 101–122, 2021.
[2] J. Seo, I. Yoon, J. Jung, J. Ryoo, J. Park, W. Lee, D. Ko, and J. Oh, "Miniaturized dual-band broadside/endfire antenna-in-package for 5g smartphone," *IEEE Trans. Antennas Propag.*, vol. 69, no. 12, pp. 8100–8114, 2021.
[3] T. S. Rappaport, Y. Xing, G. R. MacCartney, A. F. Molisch, E. Mellios, and J. Zhang, "Overview of millimeter wave communications for fifth-generation (5g) wireless networks—with a focus on propagation models," *IEEE Trans. Antennas Propag.*, vol. 65, no. 12, pp. 6213–6230, 2017.
[4] M. Xue, W. Wan, Q. Wang, and L. Cao, "Low-profile wideband millimeter-wave antenna-in-package suitable for embedded organic substrate package," *IEEE Trans. Antennas Propag.*, vol. 69, no. 8, pp. 4401–4411, 2021.
[5] G. Kim and S. Kim, "Design and analysis of dual polarized broadband microstrip patch antenna for 5g mmwave antenna module on fr4 substrate," *IEEE Access*, vol. 9, pp. 64 306–64 316, 2021.

[6] B. Kim, J. Jung, S. Yun, H. Kim, and J. Oh, “Heterogeneous metasurface empowering proximate high-permittivity ceramic cover for a 5g dual-band millimeter-wave smartphone,” *IEEE Trans. Antennas Propag.*, vol. 72, no. 5, pp. 4086–4094, 2024.

[7] R. Liu, G. Yu, J. Yuan, and G. Y. Li, “Resource management for millimeter-wave ultra-reliable and low-latency communications,” *IEEE Trans. Commun.*, vol. 69, no. 2, pp. 1094–1108, 2021.

[8] J. Kim, Y.-J. Choi, G. Noh, and H. Chung, “On the feasibility of remote driving applications over mmwave 5g vehicular communications: Implementation and demonstration,” *IEEE Trans. Veh. Technol.*, vol. 72, no. 2, pp. 2009–2023, 2023.

[9] T. K. Vu, C.-F. Liu, M. Bennis, M. Debbah, M. Latva-aho, and C. S. Hong, “Ultra-reliable and low latency communication in mmwave-enabled massive mimo networks,” *IEEE Commun. Lett.*, vol. 21, no. 9, pp. 2041–2044, 2017.

[10] T.-H. Lin, K. Kanno, A. O. Watanabe, P. M. Raj, R. R. Tummala, M. Swaminathan, and M. M. Tentzeris, “Broadband and miniaturized antenna-in-package (aip) design for 5g applications,” *IEEE Antennas Wireless Propag. Lett.*, vol. 19, no. 11, pp. 1963–1967, 2020.

[11] Y. Lee, D. Ha, K. Baek, J. Lee, S. Park, J. Park, J. Heo, and J. H. Kim, “Packaging and antenna-assembled hybrid stacked pcb with novel vertical transition for 39 ghz 5g base stations,” *J. Electromagn. Eng. Sci*, vol. 24, no. 1, pp. 26–33, 2024. [Online]. Available: https://www.jees.kr/journal/view.php?number=3638

[12] S.-C. Hsieh, H.-S. Huang, W.-C. Hsiao, S.-M. Wang, and C.-Y. Ho, “Design of dual-band (28/39ghz) antenna-in-package with broad bandwidth for 5g millimeter-wave application,” *2022 IEEE 24th Electron. Packag. Technol. Conf. (EPTC)*, pp. 32–35, 2022.

[13] C.-Y.-D. Sim, J.-J. Lo, and Z. N. Chen, “Design of a broadband millimeter-wave array antenna for 5g applications,” *IEEE Antennas Wireless Propag. Lett.*, vol. 22, no. 5, pp. 1030–1034, 2023.

[14] J. Oh, B. Kim, S. Yoon, K. Kim, E. J. Sung, and J. Oh, “High-gain millimeter-wave antenna-in-display using non-optical space for 5g smartphones,” *IEEE Trans. Antennas Propag.*, vol. 71, no. 2, pp. 1458–1468, 2023.

[15] B. Kim, D. Lee, and W. Hong, “mmwave mobile devices with reconfigurable broadside and endfire radiation using shared aperture antenna-on-display and antenna-in-package,” in *2023 International Workshop on Antenna Technology (iWAT)*, 2023, pp. 1–4.

[16] H. Kim and J. Oh, “140-ghz wideband array antenna-in-package using multimode resonance,” *IEEE Trans. Antennas Propag.*, vol. 71, no. 3, pp. 2136–2144, 2023.

[17] J. Choi, D. Choi, J. Lee, W. Hwang, and W. Hong, “Adaptive 5g architecture for an mmwave antenna front-end package consisting of tunable matching network and surface-mount technology,” *IEEE Trans. Compon., Packag., Manuf. Technol.*, vol. 10, no. 12, pp. 2037–2046, 2020.

[18] J. Guo, Y. Hu, and W. Hong, “A 45° polarized wideband and wide-coverage patch antenna array for millimeter-wave communication,” *IEEE Trans. Antennas Propag.*, vol. 70, no. 3, pp. 1919–1930, 2022.

[19] Y. He, S. Lv, L. Zhao, G.-L. Huang, X. Chen, and W. Lin, “A compact dual-band and dual-polarized millimeter-wave beam scanning antenna array for 5g mobile terminals,” *IEEE Access*, vol. 9, pp. 109 042–109 052, 2021.

[20] W. Sun, Y. Li, L. Chang, H. Li, X. Qin, and H. Wang, “Dual-band dual-polarized microstrip antenna array using double-layer gridded patches for 5g millimeter-wave applications,” *IEEE Trans. Antennas Propag.*, vol. 69, no. 10, pp. 6489–6499, 2021.

[21] L.-X. Cui, X.-H. Ding, W.-W. Yang, L. Guo, L.-H. Zhou, and J.-X. Chen, “Communication compact dual-band hybrid dielectric resonator antenna for 5g millimeter-wave applications,” *IEEE Trans. Antennas Propag.*, vol. 71, no. 1, pp. 1005–1010, 2023.

[22] Z. Siddiqui, M. Sonkki, K. Rasilainen, J. Chen, M. Berg, M. E. Leinonen, and A. Pärssinen, “Dual-band dual-polarized planar antenna for 5g millimeter-wave antenna-in-package applications,” *IEEE Trans. Antennas Propag.*, vol. 71, no. 4, pp. 2908–2921, 2023.

[23] Q. Liu, H. Liu, W. He, and S. He, “A low-profile dual-band dual-polarized antenna with an amc reflector for 5g communications,” *IEEE Access*, vol. 8, pp. 24 072–24 080, 2020.

[24] S. M. Bowers, A. Safaripour, and A. Hajimiri, “Dynamic polarization control,” *IEEE J. Solid-State Circuits*, vol. 50, no. 5, pp. 1224–1236, 2015.

[25] T. H. Jang, K. K. Hwang, G. H. Park, H. Y. Kim, H. H. Bae, C. W. Byeon, and C. S. Park, “A 60 ghz wideband, low-power active receiving antenna with adjustable polarization for snr improvement,” *IEEE Trans. Antennas Propag.*, vol. 67, no. 12, pp. 7296–7303, 2019.

[26] S. Yamada, D. Choudhury, C. Thakkar, A. Chakrabarti, K. Dasgupta, S. Daneshgar, and B. D. Horine, “Cross-polarization discrimination and port-to-port isolation enhancement of dual-polarized antenna structures enabling polarization mimo,” *IEEE Antennas Wireless Propag. Lett.*, vol. 18, no. 11, pp. 2409–2413, 2019.

[27] X. Tan, X. Mei, and K.-L. Wu, “Xpd enhancement of dipole antenna arrays by inducing coherent current from feeding line,” *IEEE Trans. Antennas Propag.*, vol. 71, no. 5, pp. 3950–3958, 2023.

[28] Y.-G. Lim, Y. J. Cho, T. Oh, Y. Lee, and C.-B. Chae, “Relationship between cross-polarization discrimination (xpd) and spatial correlation in indoor small-cell mimo systems,” *IEEE Wireless Commun. Lett.*, vol. 7, no. 4, pp. 654–657, 2018.

[29] Y. Luo, Q.-X. Chu, and D.-L. Wen, “A plus/minus 45 degree dual-polarized base-station antenna with enhanced cross-polarization discrimination via addition of four parasitic elements placed in a square contour,” *IEEE Trans. Antennas Propag.*, vol. 64, no. 4, pp. 1514–1519, 2016.

[30] Y. Jin and S. Hong, “28-ghz in-band full-duplex power amplifier integrated with an impedance matched hybrid transformer,” *IEEE Microw. Wireless Compon. Lett.*, vol. 30, no. 4, pp. 410–413, 2020.

[31] C.-X. Mao, S. Gao, and Y. Wang, “Dual-band full-duplex tx/rx antennas for vehicular communications,” *IEEE Trans. Veh. Technol.*, vol. 67, no. 5, pp. 4059–4070, 2018.

[32] W. Park, C. Ahn, I. Kim, and S. Oh, “Design of a switchplexer based on a microstrip ring resonator with single-switch operation,” *J. Electromagn. Eng. Sci*, vol. 16, no. 1, pp. 29–34, 2016. [Online]. Available: https://www.jees.kr/journal/view.php?number=3217

[33] X.-H. Ding, W.-W. Yang, W. Qin, and J.-X. Chen, “A broadside shared aperture antenna for (3.5, 26) ghz mobile terminals with steerable beam in millimeter-waveband,” *IEEE Trans. Antennas Propag.*, vol. 70, no. 3, pp. 1806–1815, 2022.

[34] B. Kim, S. Bahrami, J. Park, M. Kim, and W. Hong, “Dual-band and dual-polarized shared-aperture phased-array antennas with enhanced beam coverage for 5g fr2 and 6g fr3,” *IEEE Trans. Antennas Propag.*, vol. 72, no. 3, pp. 2069–2082, 2024.

[35] C.-X. Mao, Z. H. Jiang, D. H. Werner, S. S. Gao, and W. Hong, “Compact self-diplexing dual-band dual-sense circularly polarized array antenna with closely spaced operating frequencies,” *IEEE Trans. Antennas Propag.*, vol. 67, no. 7, pp. 4617–4625, 2019.

[36] S. Priya, K. Kumar, S. Dwari, and M. K. Mandal, “Circularly polarized self-diplexing siw cavity backed slot antennas,” *IEEE Trans. Antennas Propag.*, vol. 68, no. 3, pp. 2387–2392, 2020.

[37] H. H. Bae, T. H. Jang, H. Y. Kim, and C. S. Park, “Broadband 120 ghz l-probe differential feed dual-polarized patch antenna with soft surface,” *IEEE Trans. Antennas Propag.*, vol. 69, no. 10, pp. 6185–6195, 2021.

[38] L.-H. Wen, S. Gao, Q. Luo, Q. Yang, W. Hu, Y. Yin, X. Ren, and J. Wu, “A wideband differentially fed dual-polarized antenna with wideband harmonic suppression,” *IEEE Trans. Antennas Propag.*, vol. 67, no. 9, pp. 6176–6181, 2019.

[39] L.-H. Wen, S. Gao, Q. Luo, Q. Yang, W. Hu, and Y. Yin, “A low-cost differentially driven dual-polarized patch antenna by using open-loop resonators,” *IEEE Trans. Antennas Propag.*, vol. 67, no. 4, pp. 2745–2750, 2019.

[40] N.-W. Liu, L. Zhu, W.-W. Choi, and J.-D. Zhang, “A novel differential-fed patch antenna on stepped-impedance resonator with enhanced bandwidth under dual-resonance,” *IEEE Trans. Antennas Propag.*, vol. 64, no. 11, pp. 4618–4625, 2016.

Jeongwoo Heo (Member, IEEE) received the B.S. degree in electronic engineering from Pusan National University, Busan, South Korea, in 2022, and the M.S. degree in electrical and computer engineering from Seoul National University, Seoul, South Korea, in 2025. His research interests include antenna-in-package (AiP) design for 5G/6G communication systems, active phased array antenna systems, development of radar systems with digital beamforming, and full-wave computational electromagnetic design and analysis.

Byeongjin Kim (Graduate Student Member, IEEE) received a B.S. degree in electrical and computer engineering from Seoul National University, Korea, in 2020, where he is currently pursuing the integrated master's and Ph.D. degree. His current research interests include display antenna, antenna-in-package, optically transparent antenna, transmitarray, reflectarray, metasurface antenna, and holographic metasurface antenna for 5G millimeter-wave, 6G upper-mid, and 6G sub-THz communication systems.

Maengchang Kang (Graduate Student Member, IEEE) received the B.S. and M.S. degrees from the Department of Electronic and Electrical Engineering from Hongik University, Seoul, South Korea, in 2015 and 2017, respectively. From 2017 to 2022, he was a research engineer with the RF/Microwave Team, LIG Nex1 Co., Ltd., Yongin, South Korea. He is currently pursuing a Ph. D. degree in the Department of Electrical and Computer Engineering at Seoul National University, Seoul, South Korea. His current research interests include active-phased array antennas and digital beamforming.

Heeyoung kim received his B.S degree in Electronic and Electrical Engineering from Hongik University, Seoul, South Korea in 2013. His research interests include the design of beamforming array antenna modules for 5G mmWave communication systems, vehicles, and mobile communications. He is currently the Senior Engineer of the Advanced Network Development Office of Doosan Corporation, South Korea.

Youngju Lee is currently the vice president of the Advanced Network Development Office of Doosan Corporation, South Korea, where he is involved in the research of mmWave antenna modules for 5G and advanced communications. From 2005 to 2018, he was a project leader at Samsung Electronics, South Korea, where he focused on 5G antenna systems in the sub-6 GHz and mmWave bands. His research interests include the design of beamforming array antennas for 5G communication systems, analysis of indoor and outdoor propagation for channel modeling, and development of various mobile and base station antenna applications using electromagnetic wave technology. He received his doctorate in electronics and electrical engineering from Pohang University of Science and Technology, Pohang, Korea, in 2005.

Jungsuek Oh (Senior Member, IEEE) received his B.S. and M.S. degrees from Seoul National University, Korea, in 2002 and 2007, respectively, and a Ph.D. degree from the University of Michigan at Ann Arbor in 2012. From 2007 to 2008, he was with Korea Telecom as a hardware research engineer, working on the development of flexible RF devices. In 2012, he was a postdoctoral research fellow in the Radiation Laboratory at the University of Michigan. From 2013 to 2014, he was a staff RF engineer with Samsung Research America, Dallas, working as a project leader for the 5G/millimeter-wave antenna system. From 2015 to 2018, he was a faculty member in the Department of Electronic Engineering at Inha University in South Korea. He is currently an Associate Professor in the School of Electrical and Computer Engineering, Seoul National University, South Korea. His research areas include mmWave beam focusing/shaping techniques, antenna miniaturization for integrated systems, and radio propagation modeling for indoor scenarios. He is the recipient of the 2011 Rackham Predoctoral Fellowship Award at the University of Michigan. He has published more than 50 technical journal and conference papers, and has served as a technical reviewer for the IEEE Transactions on Antennas and Propagation, IEEE Antenna and Wireless Propagation Letters, and so on. He has served as a TPC member and as a session chair for the IEEE AP-S/USNC-URSI and ISAP. He has been a senior member of IEEE since 2017.